Supporting Information for

Direct Carbonate Electrolysis into Pure Syngas

Yurou Celine Xiao,[a] Christine M. Gabardo,[a] Shijie Liu,[a] Geonhui Lee,[b] Yong Zhao,[a] Colin P. O'Brien,[a] Rui Kai Miao,[a] Yi Xu,[a] Jonathan P. Edwards,[a] Mengyang Fan,[a] Jianan Erick Huang,[b] Jun Li, [a] Panagiotis Papangelakis,[a] Tartela Alkayyali,[a] Armin Sedighian Rasouli,[b] Jinqiang Zhang,[ab] Edward H. Sargent[b] and David Sinton*[a]

[a] Department of Mechanical and Industrial Engineering, University of Toronto, 5 King's College Road, Toronto, ON M5S 3G8, Canada.

[b] Department of Electrical and Computer Engineering, University of Toronto, 10 King's College Road, Toronto, ON M5S 3G4, Canada

*Corresponding author: dave.sinton@utoronto.ca

Supplementary Note 1. Calculation of Faradaic efficiency (FE) and full cell energy efficiency (EE)

The FE of each gas product (i) was calculated by the equation below:

$$FE_{\mathrm{i}} = x_{\mathrm{i}} \times \frac{z_{\mathrm{i}} F P_0}{R T_0} \times \dot{V} \times \frac{1}{I_{\mathrm{total}}} \times 100\% \quad \text{(S1)}$$

where x_{i} is the volume fraction of the gas product i, z_{i} is the number of electrons required to produce one molecule of the product i, F is the Faraday constant (96485 s A mol^{-1}), P_0 is the pressure (101325 Pa), R is the ideal gas constant (8.314 Pa m^3 mol^{-1} K^{-1}), T_0 is the temperature (298.15 K), $\dot{V}$ is the gas flow rate at the cathode outlet, and I_{total} is the total applied current.

In all experiments, carbon monoxide (CO) and hydrogen (H_2) were the major cathodic products. The FE for methane (CH_4) was typically < 0.2%. No CO_2, other gas products, or liquid products were detected.

The EE for syngas was calculated by the equation below:

$$EE_{\mathrm{syngas}} = \frac{E^{\circ}_{\mathrm{CO}}}{E_{\mathrm{cell}}} \times FE_{\mathrm{CO}} + \frac{E^{\circ}_{\mathrm{H_2}}}{E_{\mathrm{cell}}} \times FE_{\mathrm{H_2}} \quad \text{(S2)}$$

$$E^{\circ}_{\mathrm{i}} = \frac{\Delta G^{\circ}_{\mathrm{i}}}{-z_{\mathrm{i}} F} \quad \text{(S3)}$$

where E°_{i} is the thermodynamic cell potential for the product i, $\Delta G^{\circ}_{\mathrm{i}}$ is the change in Gibbs free energy for the overall reaction with oxygen evolution reaction on the anode side, and E_{cell} is the non-iR-corrected applied voltage. Intermediate values used in EE calculation can be found in Table 1 below.

Table 1: Gibbs free energy and thermodynamic cell potential for CO and H_2

	CO	**H_2**
ΔG° (kJ/mol)	257.2	237.1
E° (V)	1.33	1.23

Supplementary Note 2. One-dimensional COMSOL multi-physics model

The carbonate electrolysis system was modelled by COMSOL Multiphysics version 5.5. The purpose of this study was to understand the relationship between chemical species concentrations and cathode local pH with different thicknesses of the CO_2 diffusion layer (CDL) (0 – 50 μm). The one-dimensional model consisted of multiple domains: a silver (Ag) catalyst (CL), a permeable CDL, a cation exchange membrane (CEM), and an anode catalyst (AL) (Fig. S3). The transport of dilute species and secondary current distribution physics modules were applied for this study. At the left boundary of the CL, a carbonate electrolyte with constant pH of 11 was supplied. This correlated to an aqueous solution of 2 M potassium ions (K^+), 0.35 M bicarbonate ions (HCO_3^-), and 0.82 M carbonate ions (CO_3^{2-}) based on carbonate equilibrium constants at 298 K.[1] At the right boundary of the AL, a constant aqueous solution of 0.05 M sulfuric acid (H_2SO_4) was supplied. The cathode potential is applied at the left boundary of the CL layer and ground is applied at the right boundary of AL. The conductivities for each domain are specified below.

The CO_2 concentration was calculated by Eq. S4 using Henry's Law (Eq. S5) and Sechenov Constant (Eq. S6). CO_2 is assumed to behave as an ideal gas and the solubility depends on pressure, temperature, and salinity.

$$C_{\mathrm{CO_2,aq}} = P_{\mathrm{CO_2}} * K_{\mathrm{H}}^{0} * K_{\mathrm{S}} \tag{S4}$$

$$\ln(K_{\mathrm{H}}^{0}) = 93.4517 \times \frac{100}{T_0} - 60.2409 + 23.3585 \times \ln\left(\frac{T_0}{100}\right) \tag{S5}$$

$$K_{\mathrm{S}} = 10^{-C_{\mathrm{K}}\left(0.0922+h_{\mathrm{G},0}\right)-C_{\mathrm{OH}}\left(0.0839+h_{\mathrm{G},0}\right)-C_{CO_3}\left(0.1423+h_{\mathrm{G},0}\right)-C_{HCO_3}\left(0.0967+h_{\mathrm{G},0}\right)} \tag{S6}$$

$C_{\mathrm{CO_2,aq}}$, C_{K}, C_{OH}, C_{CO_3}, and C_{HCO_3} represent the local concentration of dissolved CO_2, potassium (K), hydroxide ions (OH^-), carbonate ions (CO_3^{2-}), and bicarbonate ions (HCO_3^-), respectively, $P_{\mathrm{CO_2}}$ is the partial pressure of CO_2 (1 atm), and $h_{\mathrm{G},0}$ is the Sechenov Constant for CO_2 (-0.0172).[2]

Ohm's Law (Eq. S7) is applied to the CL, CDL, CEM and AL. Poisson Equation (Eq. S8) is used to model the electroneutrality and space charge of the membrane. Specifically, the CL domain consists of 60% (v/v) electrolyte with 4.56 S m^{-1} electrical conductivity and 40% (v/v) electrode with 0.8E5 S m^{-1} electrical conductivity. The AL domain consists of 90% (v/v) electrolyte with 4.56 S m^{-1} electrical conductivity and 10% (v/v) electrode with 1.4E7 S m^{-1} electrical conductivity. The CDL and CEM have electrical conductivities of 4.56 S m^{-1} and 24.92 S m^{-1}, respectively.[3] The electromigration of the charged species (proton (H^+), OH^-, CO_3^{2-}, and HCO_3^-) (V) was governed by the electrolyte induced electric field potential, electroneutrality, and the space charge of the membrane (Eq. S9).

$$i = -\sigma \frac{\partial \phi}{\partial x} \tag{S7}$$

$$\varepsilon_0 \varepsilon_{\mathrm{r}} \frac{\partial \psi}{\partial x} = F \sum z_{\mathrm{i}} C_{\mathrm{i}} + \rho_{\mathrm{CEM}} \tag{S8}$$

$$V = \phi + \psi \quad \text{(S9)}$$

where i is the applied current density (50 – 300 mA cm^{-2}), σ is the electrical conductivity, ϕ is the electric field potential, x is the thickness, ε_0 and ε_r represent the vacuum permittivity (8.8542E-12 F m^{-1}) and the relative permittivity of water (80), respectively, ψ is the electric potential due to electroneutrality and the space charge of the membrane, z_i is the charge of species i, C_i is the concentration of species i, and ρ_{CEM} is the space charge of the membrane (-1 M).

The chemical equations of CO_2 electroreduction of CO (Eq. S10), hydrogen evolution reaction (Eq. S11), and oxygen evolution reaction (Eq. S12) are listed below:

$$CO_2 + H_2O + 2e^- \rightarrow CO + 2OH^- \quad \text{(S10)}$$

$$2H_2O + 2e^- \rightarrow H_2 + 2OH^- \quad \text{(S11)}$$

$$2H_2O \rightarrow O_2 + 4H^+ + 4e^- \quad \text{(S12)}$$

Carbonate equilibrium chemical reactions (Eq. S13-S15) and water dissociation (Eq. S16) are also considered in the COMSOL model. The kinetic reaction rate constants were determined by the temperature and salinity, similar to previous literature.[4]

$$HCO_3^- \leftrightarrow H^+ + CO_3^{2-} \quad \text{(S13)}$$

$$HCO_3^- + OH^- \leftrightarrow CO_3^{2-} + H_2O \quad \text{(S14)}$$

$$CO_{2,aq} + OH^- \leftrightarrow HCO_3^- \quad \text{(S15)}$$

$$H_2O \leftrightarrow H^+ + OH^- \quad \text{(S16)}$$

The electrochemical reaction rates were calculated using the Faradaic efficiency obtained from experimental results (Eq. S17-S19).

$$r_{CO} = -\frac{i}{F} \times \left(\frac{FE_{CO}}{2}\right) \times \frac{\varepsilon_{CL}}{L_{CL}} \quad \text{(S17)}$$

$$r_{OH^-} = \frac{i}{F} \times \frac{\varepsilon_{CL}}{L_{CL}} \quad \text{(S18)}$$

$$r_{H^+} = \frac{i}{F} \times \frac{\varepsilon_{AL}}{L_{AL}} \quad \text{(S19)}$$

where r_{CO}, r_{OH^-}, and r_{H^+} are the production rates of CO, OH^-, and H^+, ε_{CL} and ε_{AL} are the porosity of the catalyst layer (0.6) and the anode layer (0.9), and L_{CL} and L_{AL} are the thickness of the electrochemically active catalyst of cathode layer and anode layer.

In the reaction-diffusion model, the species transport equations (Eq. S20 and S21) were governed by the Nernst-Planck set of equations. The Millington and Quirk set of equations (Eq. S22 and S23) were applied to calculate the effective diffusivity of species.

$$\frac{\partial C_{\mathrm{i}}}{\partial t} + \frac{\partial i_{\mathrm{i}}}{\partial x} + r_{\mathrm{i}} = R_{\mathrm{i}} \tag{S20}$$

$$J_{\mathrm{i}} = -\frac{D_{\mathrm{i}} \partial C_{\mathrm{i}}}{\partial x} - \frac{z_{\mathrm{i}} D_{\mathrm{i}}}{RT_0} F C_{\mathrm{i}} \frac{\partial V}{\partial x} \tag{S21}$$

$$\tau_{\mathrm{F,j}} = \varepsilon_{\mathrm{j}}^{-\frac{1}{3}} \tag{S22}$$

$$D_{\mathrm{i}} = \frac{\varepsilon_{\mathrm{i}}}{\tau_{\mathrm{F,i}}} D_{\mathrm{F,i}} \tag{S23}$$

where r_{i} is the production rate of species i, R_{i} is the sum of the equilibrium reactions, J_{i} is the molar flux of species i, D_{i} is the diffusion coefficient of species i, $\tau_{\mathrm{F,j}}$ is the tortuosity of the fluid for layer j, ε_{j} is the porosity of layer j (0.6 for the CL, 0.5 for the CDL, 0.1 for the CEM, and 0.9 of the AL), and $D_{\mathrm{F,i}}$ is the fluid diffusion of species i (Table 2).

Table 2: Fluid diffusion coefficient and charge for aqueous species.[5]

Species	$D_{\mathrm{F,i}}$ ($m^2\ s^{-1}$)	Charge
HCO_3^-	1.19 x 10^{-9}	-1
CO_3^{2-}	9.23 x 10^{-10}	-2
OH^-	5.29 x 10^{-9}	-1
H^+	9.31 x 10^{-9}	+1
K^+	1.96 x 10^{-9}	+1
CO_2	1.91 x 10^{-9}	0

Supplementary Note 3. Investigation of CDL induced ΔpH

We compared the full cell voltage of the zero-gap configuration to an otherwise identical system with a 25 μm CDL to investigate the effect of the CDL on the cathode pH. On the cathode side, carbonate electrolyte was recirculated. Non-CO_2-selective electrocatalysts were utilized on the cathode to constrain the product to H_2. Since CO_2 reduction to CO and HER have different thermodynamic potentials, this ensured the thermodynamic voltage of both configurations were the same and not subjected to the FE towards a particular product. The full cell voltage was also iR compensated due to the added ohmic resistance of the CDL. This ensured the difference in voltage between the two systems could be only attributed to cathode and anode overpotential, Nernstian pH losses, and other polarization losses. The two systems had identical anode and cathode catalyst, electrolytes, and reactions. Therefore, the electrode overpotential and other polarization losses are assumed to be identical and the difference between the full cell voltages were attributed to the cathode pH difference calculated by Eq. S24 (Fig. S8). Similar methods were used to investigate cathode pH shifts in gaseous CO_2 systems.[6,7]

$$\Delta pH = \frac{\Delta \text{Voltage}}{0.059\ \text{V}} \tag{S24}$$

Supplementary Note 4. Comparison of syngas production methods

The energy intensity and carbon emissions of three direct air capture to syngas production methods were analyzed and summarized in Table 3 and Table 4.

CO_2 Capture

In all cases, CO_2 was initially captured from the air using an alkaline capture liquid which require a fluid pump and a fan to drive the air.[8] For syngas pathways requiring a feedstock of gaseous CO_2, additional CO_2 capture processes are considered: pellet formation, calcination, slaking, CO_2 dehydration and compression, and air separation for natural gas combustion. The calciner operates at 900°C and is powered by natural gas combustion. All other processes are assumed to be powered by renewable electricity.

Reverse Water Gas Shift (rWGS)

The rWGS reaction is a well-established process that converts H_2 and CO_2 into CO and water. Due to the thermodynamic limitations of the rWGS reaction and the competing Sabatier reaction that converts CO_2 into CH_4, the rWGS process needs to be run at elevated temperatures and pressures to achieve a high CO yield.[9] It is assumed that natural gas is used to power this process due to the high temperatures required (850 – 900°C). Using a mole fraction of 0.35 CO_2 and 0.65 H_2 in the feedstock, a syngas with H_2/CO ratio of 1 was obtained.[10] CO_2 in the rWGS reactor outlet was recovered using an amine unit and excess water was removed. The H_2 required for rWGS was produced using high temperature water electrolysis (HT-WE).[11]

Low Temperature CO_2 Electrolysis and Water Electrolysis (CE-WE)

High Faradaic efficiencies towards CO (< 95%) at low electrolyzer overpotentials (< 3 V full cell) have been achieved via low temperature electrolysis of CO_2.[12] The energy of CO_2 electrolysis and recovery of excess CO_2 in the gas outlet via monoethanolamine absorption was considered.[13] It is assumed that the CO_2 electrolyzer has a 25% utilization efficiency.[14,15] H_2 was produced via low temperature water electrolysis (LT-WE), calculated using commercially available water electrolyzers with > 400 $nm^3\ h^{-1}$ capacity.[16] A H_2/CO ratio of 1.16 was obtained by mixing CO and H_2. Excess water vapour was removed via TEG absorption.[17]

Direct Carbonate Electrolysis (DCE)

The CO_2 and water electrolysis energy to produce syngas using DCE is calculated by the equation below:

$$Electrolysis\ Energy_{\text{syngas}} = \frac{\Delta G^{\circ}_{\text{CO}} \times FE_{\text{CO}} + \Delta G^{\circ}_{\text{H}_2} \times FE_{\text{H}_2}}{EE_{\text{syngas}}} \quad \text{(S25)}$$

Syngas produced at 200 mA cm^{-2}, with full cell voltage of 3.79 V, and H_2/CO ratio of 1.16 (CO FE 46.4%) was used in this energy analysis. Excess water vapour was removed from the DCE gas outlet via TEG absorption.[17]

CO_2e Emissions

The CO_2e emissions for natural gas combustion is 486 $gCO_2e\ kWh^{-1}$ (0.135 $tCO_2e\ GJ^{-1}$).[18] The CO_2e emissions for renewable energy is assumed to be 25 $gCO_2e\ kWh^{-1}$ (0.007 $tCO_2e\ GJ^{-1}$), an average of 6 renewable electricity sources: photovoltaic, concentrated solar, geothermal, hydropower, ocean, and wind.[19] It is assumed that processes requiring high temperatures (900°C) will be powered by natural gas and all other processes are powered by renewable electricity (< 200°C).

Table 3: Energy breakdown for syngas production through rWGS, CE-WE, and DCE

Process	**rWGS ($GJ\ tsyngas^{-1}$)**	**CE-WE ($GJ\ tsyngas^{-1}$)**	**DCE ($GJ\ tsyngas^{-1}$)**	**References**
CO_2 Capture	10.36	9.53	0.43	[8]
WE	19.86	14.21		[11,16]
rWGS	8.01			[10]
CE		19.40		[12]
CO_2 Recovery	18.08	16.97		[10,13]
DCE			51.92	This work
Dehydration	0.63	0.01	0.01	[10,17]
Total	**56.95**	**60.13**	**52.37**	

Table 4: CO_2e emissions for syngas production through rWGS, CE-WE, and DCE

Process	**rWGS ($tCO_2e\ tsyngas^{-1}$)**	**CE-WE ($tCO_2e\ tsyngas^{-1}$)**	**DCE ($tCO_2e\ tsyngas^{-1}$)**
CO_2 Capture (calcination)*	1.118	1.028	
CO_2 Capture (all other processes)	0.014	0.013	0.003
WE	0.138	0.099	
rWGS*	1.082		
CE		0.135	
CO_2 Recovery	0.126	0.118	
DCE			0.361
Dehydration	0.004	1.0E-04	1.0E-04
Total	**2.482**	**1.393**	**0.364**

*****These processes are assumed to be powered by natural gas

Table 5: Typical carbonate electrolyte flowrates at various current densities

Current Density ($mA\ cm^{-2}$)	**Typical carbonate electrolyte flowrate ($mL\ min^{-1}$)**
50	12.5
100	15
150	17.5
200	20
250	25
300	30

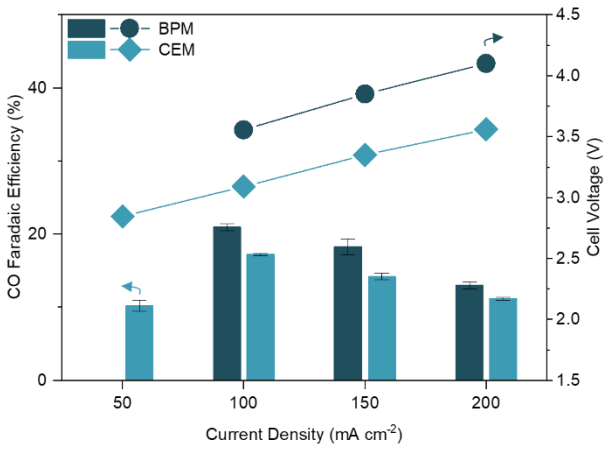

Fig. S1 FE towards CO in a zero-gap configuration using a bipolar membrane (BPM) at current densities between 100 to 200 mA cm^{-2} and a cation exchange membrane (CEM) at current densities between 50 to 200 mA cm^{-2}. Corresponding full cell voltages are noted on the secondary y-axis. Error bars represent the standard deviation of at least three samples measured under identical conditions.

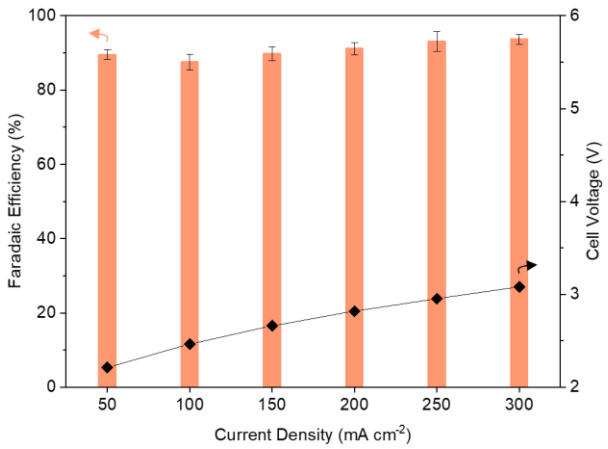

Fig. S2 FE towards H_2 in a zero-gap configuration using a CEM and 1M KOH as the anolyte at current densities between 50 to 300 mA cm^{-2}. No other products were detected. Corresponding full cell voltages are noted on the secondary y-axis. Error bars represent the standard deviation of at least three samples measured under identical conditions.

Fig. S3 Schematic of the one-dimensional model with the thickness of each component indicated. X = 0 represents where the Distance from Cathode is calculated from in all modelling figures.

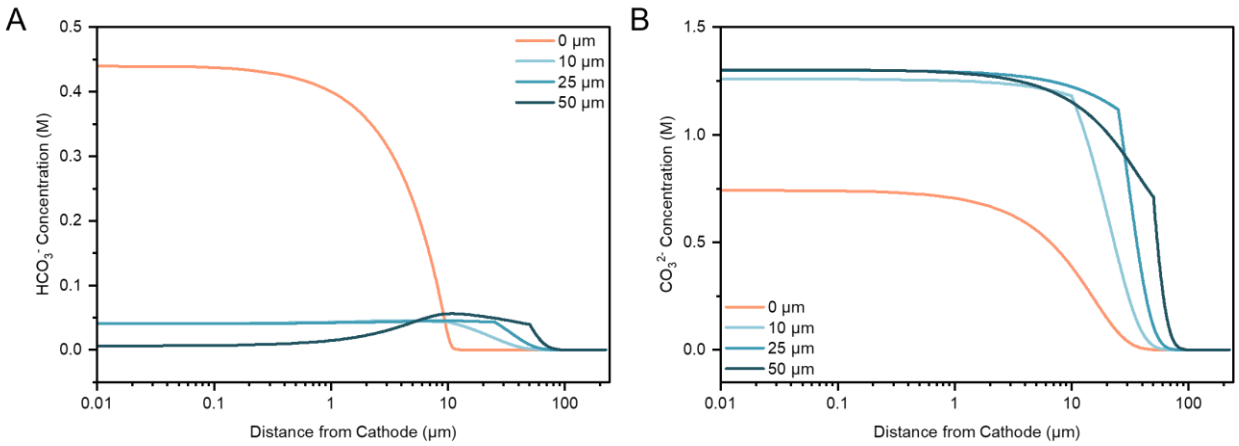

Fig. S4 One-dimensional multi-physics modelling of HCO_3^- **(A)** and CO_3^{2-} **(B)** concentrations at distances from the cathode and current density of 200 mA cm^{-2} for CDL with thickness of 0 (zero-gap), 10, 25, and 50 µm.

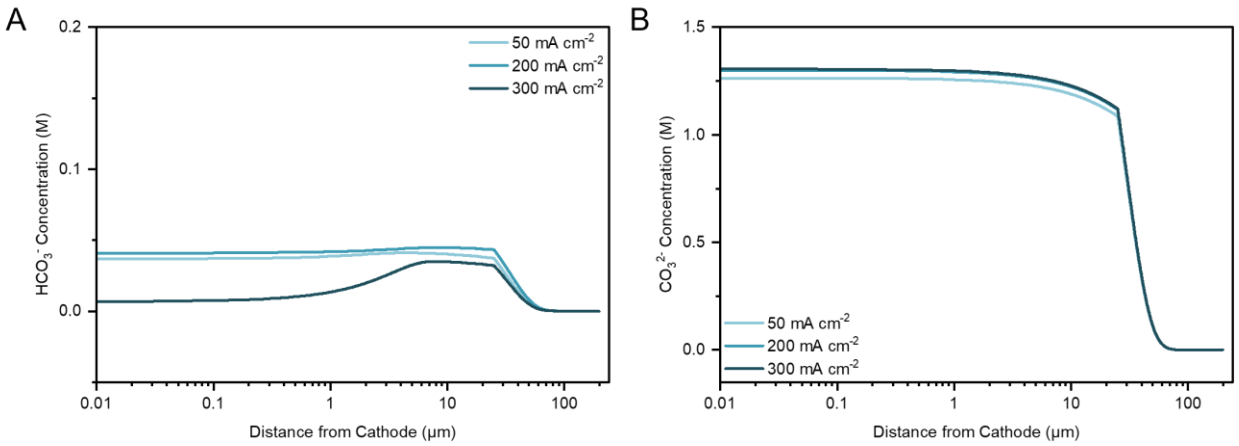

Fig. S5 One-dimensional multi-physics modelling of HCO_3^- **(A)** and CO_3^{2-} **(B)** concentration at distances from the cathode and current densities of 50, 200, and 300 mA cm^{-2} for 25 μm CDL.

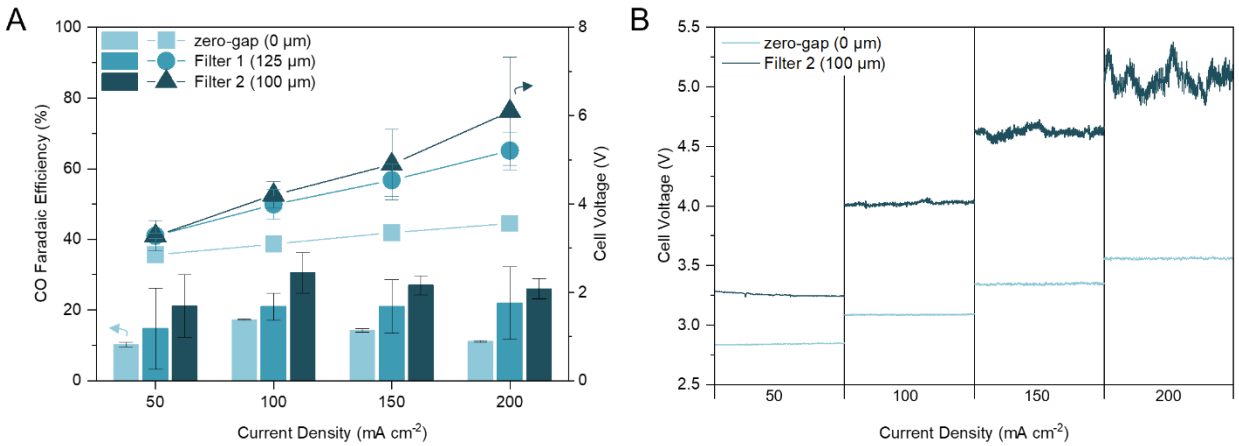

Fig. S6 Comparison of FE and cell voltage of inserted hydrophilic microporous filters and the zero-gap configuration. **(A)** FE towards CO at current densities between 50 to 200 mA cm^{-2} for the zero-gap configuration, a 125 µm PVDF filter (Filter 1), and a 100 µm nylon filter (Filter 2). Corresponding full cell voltages are noted on the secondary y-axis. Error bars represent the standard deviation of at least three samples measured under identical conditions. **(B)** Non-iR-corrected full cell voltage of a zero-gap configuration and a Filter 2 experiment at current densities of 50, 100, 150, and 200 mA cm^{-2}. For each current density, the voltage data shown is a representative subset that spans over 300 seconds of continuous operation. Large voltage fluctuations for Filter 2, especially at 200 mA cm^{-2}, indicate trapped gaseous bubbles.

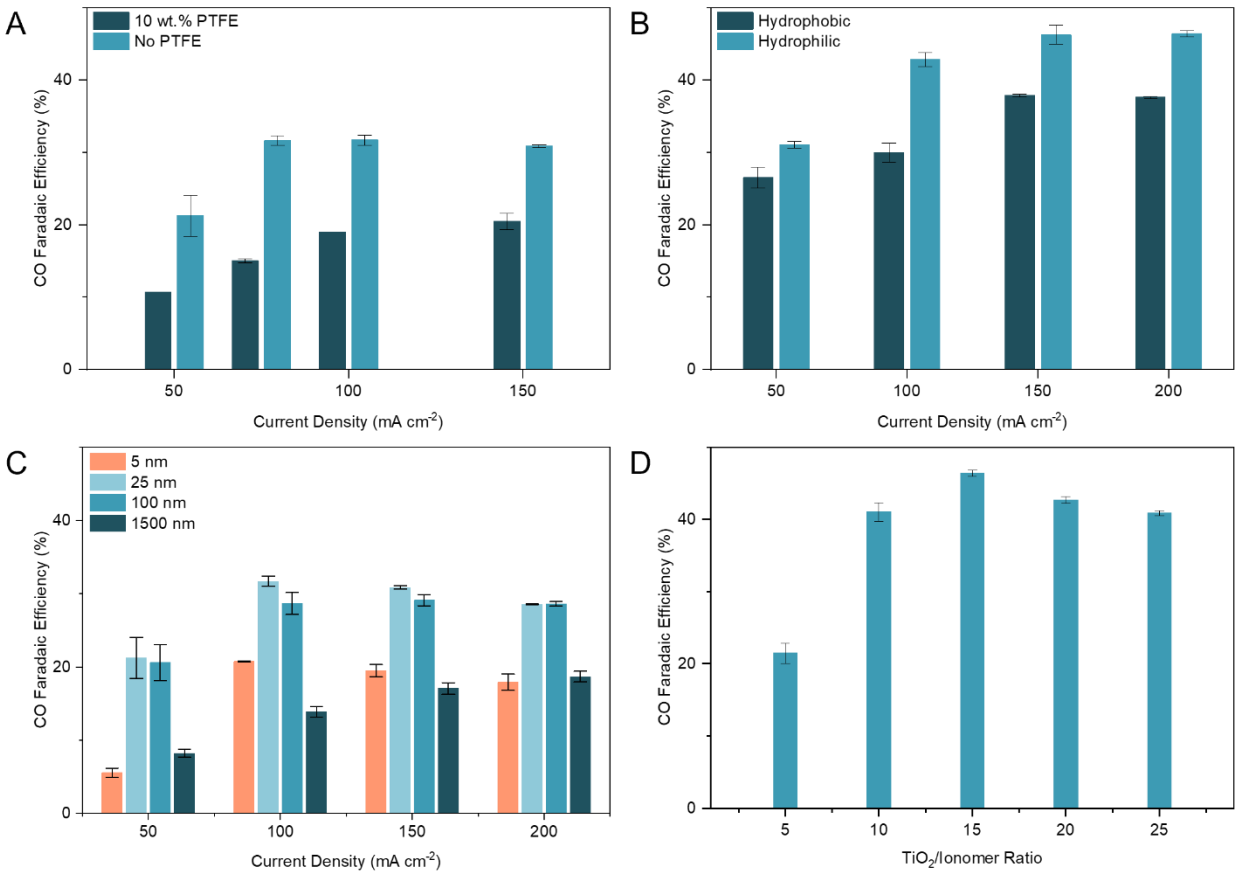

Fig. S7 FE towards CO for various CDL compositions. **(A)** FE towards CO at current densities between 50 to 150 mA cm^{-2} for CDL containing TiO_2 with 10 wt.% hydrophobic PTFE mixed in and with no PTFE. **(B)** FE towards CO at current densities between 50 to 200 mA cm^{-2} for CDLs using Nafion as the ionomer (Hydrophobic) and using Aemion as the ionomer (Hydrophilic). **(C)** FE towards CO at current densities between 50 to 200 mA cm^{-2} for CDLs using different sizes of TiO_2: 5, 25, 100, and 1500 nm and TiO_2/ionomer ratio of 25. **(D)** FE towards CO at 200 mA cm^{-2} for CDLs with different TiO_2/ionomer weight ratios between 5 to 25 and TiO_2 size of 25 nm. Error bars represent the standard deviation of at least three samples measured under identical conditions.

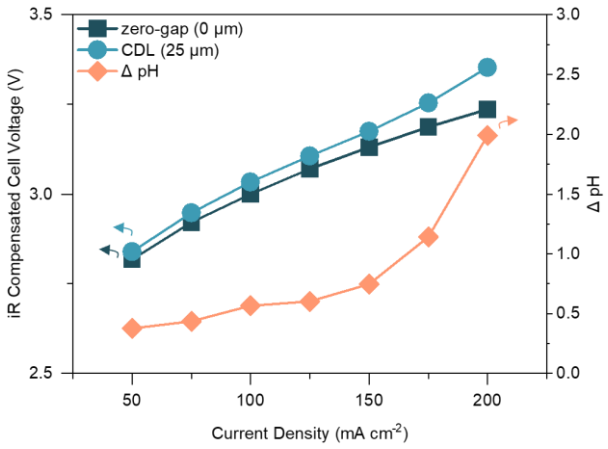

Fig. S8 iR-compensated full cell voltage for HER on the cathode for a zero-gap configuration and with a 25 µm CDL. Corresponding pH difference (ΔpH) calculated by Eq. S24 is noted on the secondary y-axis.

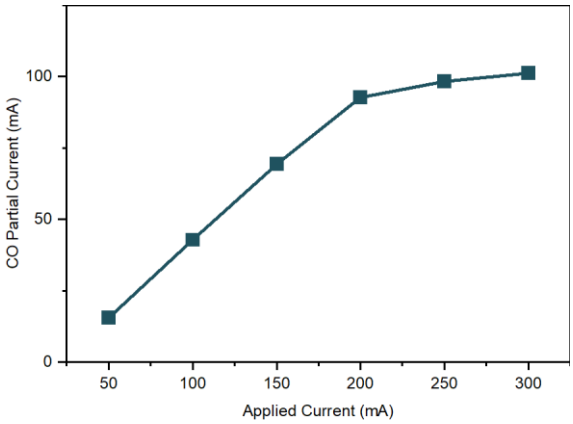

Fig. S9 CO partial current for the optimized 25 µm CDL at current densities between 50 to 300 mA cm^{-2}.

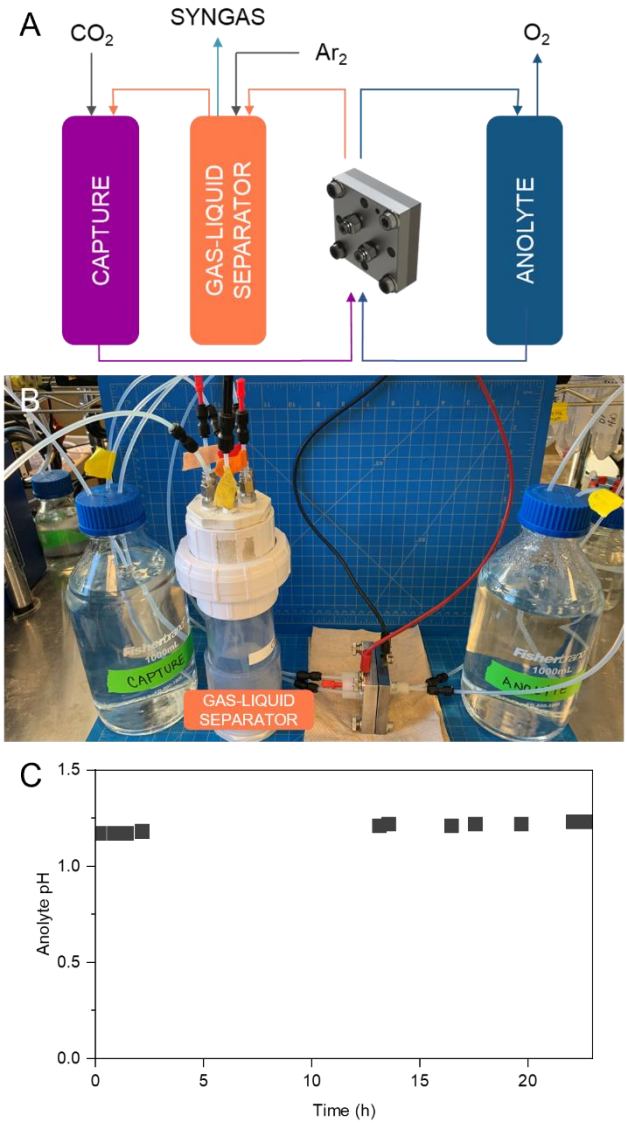

Fig. S10 Long-term stability experiment. **(A)** Schematic of the stability experiment which includes a capture container fed with CO_2 gas, an airtight gas-liquid separator purged with Ar_2 gas for gas product analysis, and an anolyte container. Liquid from the gas-liquid separator is recycled to the capture container. **(B)** Picture of the stability experiment. **(C)** pH of anolyte over time.

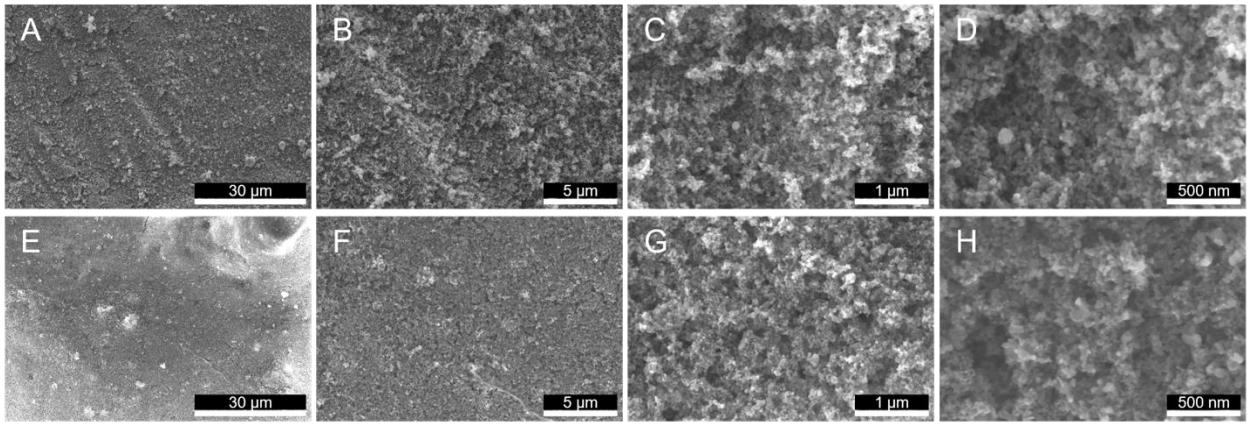

Fig. S11 Scanning electron microscopy (SEM) images of the CDL before **(A-D)** and after **(E-H)** prolonged operation.

References

1 I. Halevy and D. P. Schrag, *Geophys. Res. Lett.*, 2009, **36**, L23201.

2 S. Weisenberger and A. Schumpe, *AIChE J.*, 1996, **42**, 298–300.

3 C. M. Gabardo, C. P. O'Brien, J. P. Edwards, C. McCallum, Y. Xu, C.-T. Dinh, J. Li, E. H. Sargent and D. Sinton, *Joule*, 2019, **3**, 2777–2791.

4 C. McCallum, C. M. Gabardo, C. P. O'Brien, J. P. Edwards, J. Wicks, Y. Xu, E. H. Sargent and D. Sinton, *Cell Reports Physical Science*, 2021, **2**, 100522.

5 Y. Xu, J. P. Edwards, S. Liu, R. K. Miao, J. E. Huang, C. M. Gabardo, C. P. O'Brien, J. Li, E. H. Sargent and D. Sinton, *ACS Energy Lett.*, 2021, **6**, 809–815.

6 C.-T. Dinh, T. Burdyny, M. G. Kibria, A. Seifitokaldani, C. M. Gabardo, F. P. García de Arquer, A. Kiani, J. P. Edwards, P. De Luna, O. S. Bushuyev, C. Zou, R. Quintero-Bermudez, Y. Pang, D. Sinton and E. H. Sargent, *Science*, 2018, **360**, 783–787.

7 C. P. O'Brien, R. K. Miao, S. Liu, Y. Xu, G. Lee, A. Robb, J. E. Huang, K. Xie, K. Bertens, C. M. Gabardo, J. P. Edwards, C.-T. Dinh, E. H. Sargent and D. Sinton, *ACS Energy Lett.*, 2021, **6**, 2952–2959.

8 D. W. Keith, G. Holmes, D. St. Angelo and K. Heidel, *Joule*, 2018, **2**, 1573–1594.

9 F. Sun, C. Yan, Z. Wang, C. Guo and S. Huang, *International Journal of Hydrogen Energy*, 2015, **40**, 15985–15993.

10 E. Rezaei and S. Dzuryk, *Chemical Engineering Research and Design*, 2019, **144**, 354–369.

11 R. Küngas, P. Blennow, T. Heiredal-Clausen, T. Holt Nørby, J. Rass-Hansen, J. B. Hansen and P. G. Moses, *ECS Trans.*, 2019, **91**, 215–223.

12 R. Küngas, *J. Electrochem. Soc.*, 2020, **167**, 044508.

13 M. R. M. Abu-Zahra, L. H. J. Schneiders, J. P. M. Niederer, P. H. M. Feron and G. F. Versteeg, *International Journal of Greenhouse Gas Control*, 2007, **1**, 37–46.

14 M. Ma, S. Kim, I. Chorkendorff and B. Seger, *Chem. Sci.*, 2020, **11**, 8854–8861.

15 B. Endrődi, E. Kecsenovity, A. Samu, T. Halmágyi, S. Rojas-Carbonell, L. Wang, Y. Yan and C. Janáky, *Energy Environ. Sci.*, 2020, **13**, 4098–4105.

16 A. Buttler and H. Spliethoff, *Renewable and Sustainable Energy Reviews*, 2018, **82**, 2440–2454.

17 M. Netusil and P. Ditl, *Journal of Natural Gas Chemistry*, 2011, **20**, 471–476.

18 P. R. O'Donoughue, G. A. Heath, S. L. Dolan and M. Vorum, *Journal of Industrial Ecology*, 2014, **18**, 125–144.

19 S. Nicholson and G. Heath, 4.